Coastal Engineering 202 (2025) 104839

Contents lists available at ScienceDirect

Coastal Engineering

journal homepage: www.elsevier.com/locate/coastaleng

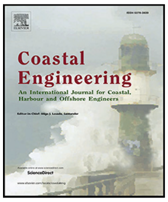

Experimental analysis of post-overtopping flows on composite vertical breakwaters with retreated wave walls: Mapping of the hydrodynamic parameters[☆]

Matteo Centorami[a], Alessandro Romano[a,b,*], Claudia Cecioni[a], Giorgio Bellotti[a]

[a] Roma Tre University, Department of Civil, Computer Science and Aeronautical Technologies Engineering, Rome 00146, Italy
[b] IHCantabria - Instituto de Hidráulica Ambiental de la Universidad de Cantabria, Calle Isabel Torres 15, Santander 39011, Spain

ARTICLE INFO

Keywords:
Vertical breakwaters
Post-overtopping flows
Wave-structure interaction
Physical model tests
Water waves

ABSTRACT

Retreated wave walls are often used to improve the hydrodynamic performance of composite vertical breakwaters placed in relatively deep-water conditions. The wall retreat changes significantly the dynamics of wave-structure interaction, making the current design criteria not adequate for such structures. Previous experimental findings highlight that these processes are governed by the complex hydrodynamics driven by the characteristics of post-overtopping flows occurring on the superstructure between the seaward edge of the caisson trunk and the wave wall. In this article a new 2D experimental campaign has been carried out to explore the hydrodynamics of post-overtopping flows on composite vertical breakwaters with retreated wave wall. To improve the overall understanding of the phenomena, these flows have been analyzed and classified into three distinct types, based on wave characteristics and structural parameters, namely: Dam break (DB), Plunging-Dam break (PDB), and Hammer-Fist (HF). Then, the characteristics of each event type have been studied as a function of the wave wall retreat position. To this end, an advanced image-clustering analysis technique has been applied to visualize the process and estimate those quantities which are difficult to measure with direct measurement techniques (e.g., air content). Moreover, wave-induced loads on the wall and downfall pressures have been measured, allowing to explore how different flow types, wall retreats, and aeration levels could affect impact loads and flow dynamics. The detailed analysis of the post-overtopping flows dynamics, combined with the measurements of the forces acting on the wave wall, allowed to obtain a comprehensive parameters map, based on the flows classification and geometrical dimensions, which contributes to the development of practical design tools for such structures.

1. Introduction

Composite vertical breakwaters are monolithic structures often used to protect harbour basins. Their use is convenient for large water depths and non-breaking wave conditions. These structures are typically composed of a rubble mound foundation, a vertical concrete caisson (trunk), and a superstructure with wave wall. Often the size of such structures is significant, therefore the improvement of their hydraulic performance (e.g., reduction of the forces acting on them and/or reduction of the reflection coefficient and/or the wave overtopping) without varying significantly the geometric dimension of the structure themselves may result in a significant economic saving.

To reduce wave loads on such structures, a common technical solution consists in placing the wave wall on a retreated position with respect to the seaside edge of the caisson trunk. Emblematic examples of this technical solution are provided by the breakwaters of two large italian harbours, namely Civitavecchia (Central Tyrrhenian Sea, Italy) and Genoa (Northern Tyrrhenian Sea, Italy; currently under construction). Note that the former is one of the largest cruise terminals in the Mediterranean Sea, while the latter, once finished, will be the second largest vertical breakwater in the world.

Currently, design criteria of composite vertical breakwaters are mainly based on the Goda's formulae (Goda, 2010), including impulsive breaking conditions proposed by Takahashi (1996). Nevertheless, the retreat of the wave wall changes significantly the wave-structure interaction dynamics, making the design criteria not adequate. Recently, Romano and Bellotti (2023) and Romano et al. (2024), have studied

---

[☆] Given his role as Associate Editor, Giorgio Bellotti had no involvement in the peer-review of this article and has no access to information regarding its peer-review. Full responsibility for the editorial process for this article was delegated to another journal editor.

[*] Corresponding author at: Roma Tre University, Department of Civil, Computer Science and Aeronautical Technologies Engineering, Rome 00146, Italy.
E-mail address: alessandro.romano@uniroma3.it (A. Romano).

https://doi.org/10.1016/j.coastaleng.2025.104839
Received 18 June 2025; Received in revised form 19 July 2025; Accepted 19 July 2025
Available online 30 July 2025
0378-3839/© 2025 The Authors. Published by Elsevier B.V. This is an open access article under the CC BY license (http://creativecommons.org/licenses/by/4.0/).

the influence of the wall retreat on the forces increase/reduction on such structures and have identified the governing physical/geometrical drivers on the basis of laboratory experiments at different scales. They pointed out that the wave forces acting on the whole structure and on the caisson trunk tend to decrease for retreated wall configurations, while those acting on the wall exhibit a general increase, often due to the occurrence of impulsive loads, regardless the value of the wall retreat. Their findings clearly highlight that the process is governed by a complex hydrodynamics, driven by the characteristics of post-overtopping flows occurring on the superstructure between the seaward edge of the trunk and the wave wall.

Historically, the hydrodynamics of post-overtopping flows has been mainly investigated in the field of naval and offshore engineering (where these flows are often called “green water” events). Specifically, several works focused on the study of the kinematic and dynamic (i.e., wave loads) properties of such flows on ships’ decks (Goda and Miyamoto, 1976; Buchner, 1995, 2002; Ryu et al., 2007; Lee et al., 2012; Song et al., 2015; Silva et al., 2017; Chen et al., 2019; Lee et al., 2020; Wang et al., 2023; Gao et al., 2025). Moreover, other studies focused on the classification of the different types of post-overtopping flows (Greco et al., 2005, 2007; Fontes et al., 2021).

These events can be mainly classified, by considering the interaction of the water flow with the deck’s edge, into three distinct categories, namely: Dam break (DB), Plunging-Dam break (PDB), and Hammer-Fist (HF). The transition between these types depends both on the wave steepness and the crest freeboard. These types, listed in order of increasing wave steepness, are differentiated on the basis of the propagation direction and on the characteristics of the flow front: (I) DB-type has mainly an horizontal component and the front is compact and low-aerated; (II) PDB-type, although having mainly an horizontal component, features a plunging-like front that induces the formation of a spherical or elliptical air cavity at the edge of the deck; (III) HF-type, occurring under very steep wave conditions, is a sub-vertical water jet that abruptly collapses onto the deck.

As far as coastal structures are concerned, post-overtopping flows are less investigated, although some studies are available especially for smooth dikes (De Finis et al., 2020; Chen et al., 2021; Neves et al., 2021; Cao et al., 2022; van Bergeijk et al., 2022a,b). To the best authors’ knowledge, there is a lack of literature on the study of post-overtopping flows on composite vertical breakwaters, especially if retreated wall configurations are used. Since, as highlighted by Romano and Bellotti (2023) and Romano et al. (2024), the wave-structure hydrodynamics of vertical breakwaters with retreated walls is governed by the characteristics of post-overtopping flows, classifying these events is expected to improve the overall understanding of the phenomena and contribute to the development of practical design tools for such structures. Moreover, the nature of the wave loads on the wall, and the related wave overtopping, has a direct influence also on the so-called “downfall pressures”, caused by the jet falling on the deck behind the wave wall. Such pressures can be also very large, as experimentally demonstrated by Wolters et al. (2005).

In this study, we present the results of a new 2D experimental campaign aiming at providing a comprehensive analysis of the post-overtopping flow events on composite vertical breakwaters with retreated wave walls. Specifically, the objectives of the work consist of investigating the characteristics of wave-induced loads on the wall and on the superstructure (i.e., downfall pressures). The methodology proposed in this article follows a two-stage approach: firstly, the classification proposed in the literature by Greco et al. (2005, 2007), Fontes et al. (2021) is used to explore the onset of these types of events on such structures. To this end, in the first stage, the experiments have been carried out without the wave wall, using regular waves by varying the governing parameters (wave height, wave period, crest freeboard, etc.), to establish a baseline characterization. In the second stage, for each type of event (DB, PDB, HF), some selected representative conditions have been reproduced by varying the wave wall position (i.e., wall retreat).

The aim of this experimental campaign is to carry out an in-depth analysis of the processes occurring within one wave period (i.e., intra-wave process). Therefore, an advanced image-clustering analysis technique has been applied to visualize the process and estimate those quantities which are difficult to measure with direct measurement techniques: e.g., air content, presence of bubbles, etc. Moreover, the wave-induced pressures, including downfall on the deck, acting on the structure are measured, exploring how different flow types, wall retreats, and aeration levels affect impact loads and flow dynamics.

The detailed analysis of the post-overtopping flows dynamics, combined with the measurements of the pressures acting on the wave wall, allows to obtain a comprehensive parameter map, based on the flows classification and on the geometrical parameters of the problem. The map, which is inspired to that developed within the PROVERBS Project (PRObabilistic design tools for VERtical BreakwaterS) and reported by Oumeraci et al. (2001), is to provide practical guidelines to design these structures.

The paper is structured as follows. After this introduction, the description of the methodology is given, covering the experimental setup and the data processing techniques (forces and image-clustering method). Then, results and discussion section follows. Finally, conclusions close the paper.

2. Methodology

2.1. Experimental setup

The 2D experiments have been carried out in the hydraulics laboratory of Roma Tre University (Department of Civil, Computer Science and Aeronautical Technologies Engineering, Rome, Italy). The laboratory is equipped with a wave flume made of steel and glass, represented in panel a) of Fig. 1. The flume is 20.0 m long, 0.605 m wide and 1.0 m high, and has a piston-type wave-maker with a maximum stroke of 1.35 m, allowing the generation of both regular and irregular waves. The wave generation system is controlled by the state of the art software AWASYS 7 (Aalborg University), which includes an active wave absorption system (Andersen et al., 2016, 2018).

The modeled structure replicates a vertical breakwater placed on top of a rubble mound foundation. Rather than replicating a specific prototype structure, the physical model is designed to represent, in Froude similarity, a broad range of vertical breakwater configurations in relatively deep water. It might roughly resemble the new vertical breakwater of the Genoa port expansion project (Mediterranean Sea, Northern Italy), considering a reduction scale of approximately 1:55.

The vertical breakwater is made by a caisson trunk and of a superstructure with a vertical wall, both made of 0.015 m thick marine plywood (see Fig. 1, panel b)). The caisson trunk is $h_t = 0.50$ m high and the crown wall is $h_w = 0.06$ m high; their width is 0.60 m to fit inside the wave flume. The caisson trunk and wall dimensions remain constant during all tests. The crown wall can be easily moved and fixed at different horizontal positions to test different wall retreats with respect to the seaward face of the caisson trunk. The rubble mound foundation is $h_b = 0.25$ m high. It is made up of two parts: an inner core of uniform-sized rock material and an external rubble mound layer made of rocks with weight range of 20.0–30.0 g, shown in Fig. 1, panel b).

Panel c) of Fig. 1 reports a sketch of the longitudinal section of the breakwater and wave gauge setup, inside the wave flume, with measures in meters. A total of seven resistive wave gauges are placed along the flume to measure the free surface elevation. Two wave gauges are mounted on the piston-type wave-maker for the active absorption system (WG1 and WG2). Five wave gauges have been aligned in the central longitudinal axis of the flume, to measure the wave field in front of the structure (WG3-WG7). The acquisition frequency of the wave

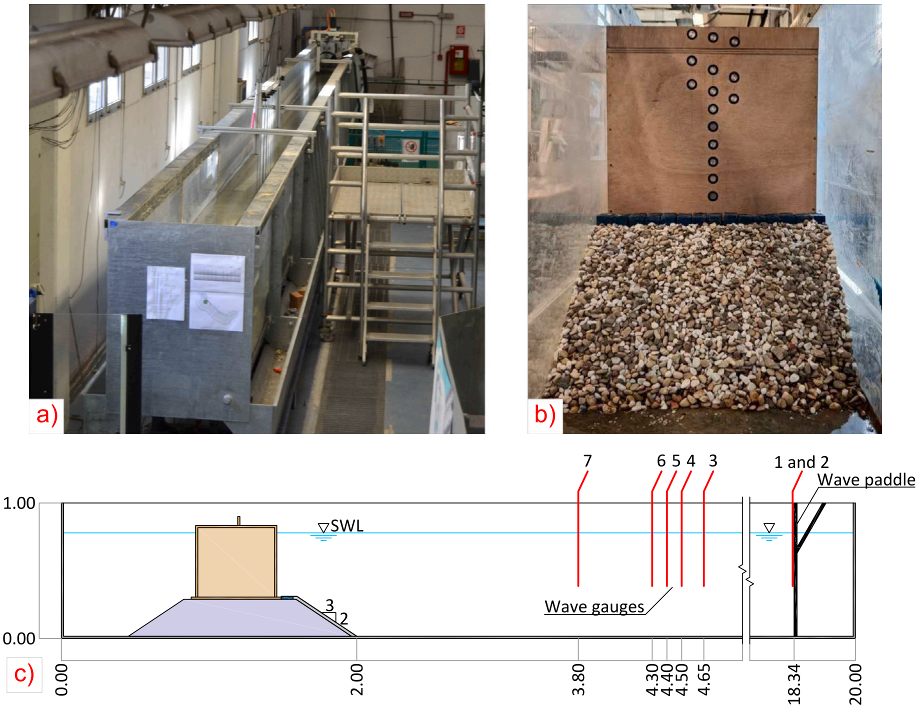

Fig. 1. Panel a): Picture of the wave flume. Panel b): Front view picture of the composite vertical breakwater model. Panel c): Longitudinal section of the model structure and wave gauges setup in the wave flume.

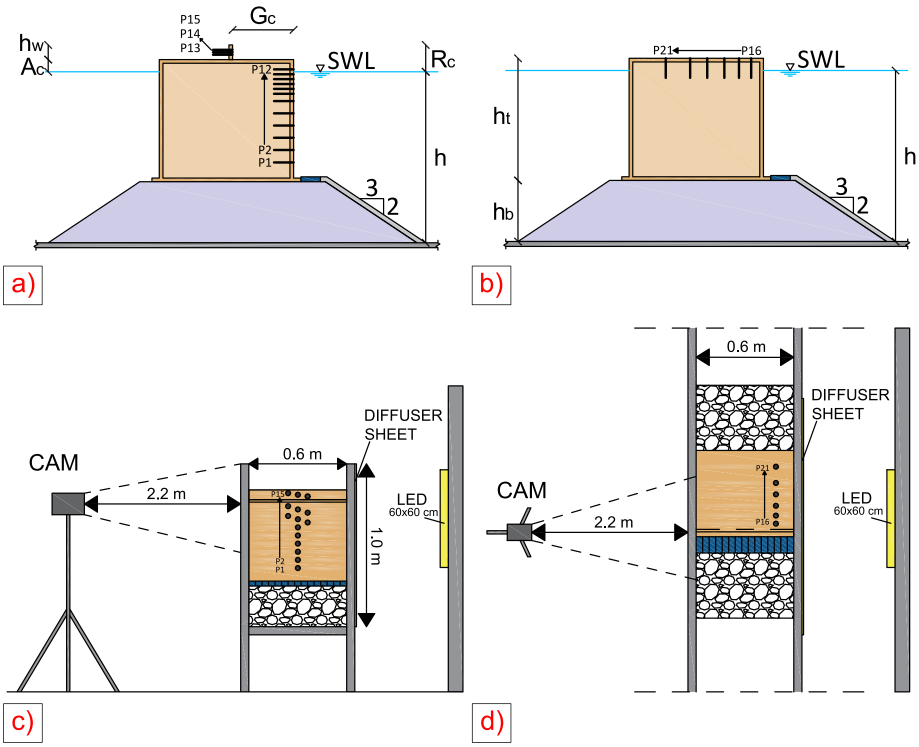

Fig. 2. Top panels: longitudinal view of the composite breakwater, with indication of the geometrical parameters and positions of the front (panel a)) and top (panel b)) pressure sensors respectively. Bottom panels: front (panel c)) and plan (panel d)) views of the experimental set-up.

gauges is set at 50 Hz, and a calibration procedure is carried out at least twice a day to account for environmental variations.

A total of 21 pressure transducers (TRAFAG Submersible Pressure Transmitter NAL 8838, with pressure range 0–200 mbar) are fixed on the structure. As illustrated in the longitudinal views in Fig. 2, panels a) and b), 12 sensors (P1-P12) are placed on the caisson trunk seawards facing, 3 (P13-P15) on the crown wall and 6 (P16-P21) on the top of the caisson to measure the pressures induced by the post-overtopping volumes of water falling on the deck of the structure (i.e., downfall pressures). The position of these sensors is also shown in panels c) and d) of Fig. 2, from a front view and a plan view, respectively. To maximize the number of sensors on the crown wall and around

Table 1
Pressure sensor names (first column), positions (second column) and areas of influence (third column). For the sensors placed on the sea-ward face of the caisson trunk (P1-P15), the position is the vertical distance from the bottom corner of the trunk. For the sensors placed on the deck (P16-P21) the position is the horizontal distance from the trunk sea-face.

Front pressure sensors		
Pressure sensor	Vertical position (m)	Influence area (m^2/m)
$P1$	0.080	0.090
$P2$	0.130	0.050
$P3$	0.180	0.050
$P4$	0.230	0.050
$P5$	0.280	0.050
$P6$	0.330	0.040
$P7$	0.360	0.025
$P8$	0.380	0.020
$P9$	0.400	0.020
$P10$	0.420	0.020
$P11$	0.440	0.020
$P12$	0.460	0.050
$P13$	0.520	0.025
$P14$	0.530	0.010
$P15$	0.540	0.025

Top pressure sensors		
Pressure Sensor	Horizontal position (m)	Influence area (m^2/m)
$P16$	0.050	0.075
$P17$	0.100	0.055
$P18$	0.160	0.065
$P19$	0.230	0.070
$P20$	0.300	0.075
$P21$	0.400	0.150

the mean sea level, the mutual vertical distance between the pressure sensors is not constant, spanning in the range 0.01 m-0.05 m. Table 1 reports the names, positions and influence area of the pressure sensors, differentiating the front sensors (P1-P15) from the top sensors (P16-P21). The acquisition frequency of all these pressure transducers is 7 kHz to accurately measure impulsive load peaks.

A particular care has been adopted in minimizing potential laboratory effects. Specifically, to equip the caisson trunk and wall with a large number of pressure measurement points and to ensure that its seaside face was as rigid and flat as possible, some special pieces (or masks) have been ad-hoc designed and 3D-printed for housing the pressure sensors. These masks, shown in panel b) of Fig. 1, ensure the perfect alignment between the pressure sensors and the vertical front face of the structure.

An optimized setup was designed to accurately video record the dynamic flow phenomena during the experiments. To this end, a camera was placed at a distance of 2.2 meters from one side the wave flume, pointing perpendicularly to the physical model (Fig. 2 panels c) and d)). To ensure consistent and clear visual data, an illumination system, composed of 60 cm x 60 cm LED panel with 45 W power, was installed on the opposite side of the wave flume with respect to the camera, providing uniform lighting across the observed area. Furthermore, a diffuser paper sheet was placed between the channel and the LED panel to evenly distribute the light and reduce reflections or shadows. This setup helped to distribute the light evenly and minimized reflections on the water surface, which was particularly important for maintaining consistent pixel intensity in the captured images. This arrangement was critical for achieving high-quality images that would be used for the segmentation of air bubbles, water, and background regions.

2.2. Test program

Table 2
Ranges of explored parameters tested during the experimental campaign.

Tests without the crown wall (N° tests = 52)		
Parameters	Min. Value	Max. Value
H (m)	0.0695	0.1830
T (s)	0.8000	1.3000
h (m)	0.6700	0.7300
H/h (–)	0.1038	0.2581
h/L_0 (–)	0.2541	0.7312
H/L_0 (–)	0.0383	0.1093
R_c/H (–)	0.1093	1.1507
h_b/h (–)	0.3425	0.3731

Tests with the crown wall (N° tests = 45)		
Parameters	Min. Value	Max. Value
H (m)	0.0790	0.1619
T (s)	0.8000	1.3000
H/h (–)	0.1129	0.2313
h/L_0 (–)	0.2655	0.7011
H/L_0 (–)	0.0394	0.0981
R_c/H (–)	0.3088	0.6329
G_c/L_0 (–)	0.0303	0.3506

Table 2 lists the ranges of the wave and structure parameters for the 97 tests performed. Regular waves were used in all tests to ensure controlled and repeatable conditions, allowing for a systematic analysis of the sea state influence without adding the complexity of irregular wave patterns. The duration of each test was approximately 80 s to obtain a wave time series long enough to reach stationary conditions acting on the structure.

As can be noted in Table 2, 52 tests were conducted varying wave conditions and water depth on the same composite vertical breakwater (h_b = 0.25 m and h_t = 0.50 m) without the crown wall. During these experiments, wave height H, wave period T and water depth h were systematically varied to explore the onset of the different types of post-overtopping flow events (DB, PDB, HF) and to establish a baseline characterization. The ranges of these parameters are reported in Table 2, along with dimensionless values. In particular, three values of water depth are tested, h = 0.67, 0.70, 0.73 m, corresponding to three values of crest freeboard R_c = 0.08, 0.05 and 0.02 m. In Table 2, L_0 is the deep water wave length, defined as $gT^2/(2\pi)$, with g the gravity acceleration. As stated, these tests were planned in a structural configuration without the retreated crown wall (in the following referred to as "baseline configuration"), to characterize at first the post-overtopping events varying the incident wave conditions.

Subsequently, among these 52 tests, 15 were selected as representative wave conditions of each post-overtopping flow type, and reproduced after installation of the wave wall on top of the structure. Specifically, three different configurations were tested, varying the horizontal position of the wall, G_c, with respect to the seaward face of the caisson: G_{c1} = 0.08 m ("small" wall retreat), G_{c2} = 0.18 m ("intermediate" wall retreat), and G_{c3} = 0.35 m ("large" wall retreat), leading to a total of 45 tests. For consistency, all these 45 tests were conducted at a fixed water depth of h = 0.70 m, as this condition exhibited the most relevant and interesting hydrodynamic interactions.

2.3. Data processing

2.3.1. Forces analysis

The approach used in this study to measure wave-induced loads on the vertical caisson and on the wave wall follows the procedure outlined in previous studies of Romano and Bellotti (2023), Romano et al. (2024). Each test includes an initial transient period, followed by a steady-wave phase of about 20 s during which the pressure signals are nearly repetitive from cycle to cycle. The recorded pressures p_i, from each sensor i are integrated according to a rectangular scheme, associating to each sensor an "influence area"- defined as half the distance above and half the distance below that sensor. Summing these contributions provides the instantaneous horizontal force on the structure:

$$F(t) = \sum_{i} p_i(t)\, \Delta A_i \tag{1}$$

where ΔA_i denotes the influence area of sensor i. By isolating the sensors placed on the trunk from those on the wave wall, it is possible to compute separate force contributions. Once these force time series are obtained, a peaks-over-threshold (POT) analysis is performed to identify the load peaks in each wave cycle. Under regular wave conditions, these peaks are generally consistent, so their average is taken to represent the peak load. Table 1 reports the names, positions and influence area of the pressure sensors.

2.3.2. Image analysis

Following the framework of Formentin et al. (2024), an image-based clustering technique was adopted to quantify the air content in the overtopping flows impacting the retreated wave wall. A Sony-FDR-AX53 camera (8.29 megapixels, 25 fps, 1920 × 1080 pixels) was placed as illustrated in Fig. 2 panels c) and d). Fig. 3 panel a) shows the region of interest (ROI) fixed for each test on the camera's images. It can be noted that it extends from the horizontal position of the crown wall toward the seaward side, encompassing the re-entry zone of reflected jets (Romano and Bellotti, 2023). Preliminary steps include static background subtraction, conversion to gray-scale, and contrast enhancement via thresholding. The effects of these transformations are shown in Fig. 3, panel b). The key step used k-means clustering to segment each frame into three classes: (i) background (darkest pixels), (ii) aerated flow regions (highest intensity), and (iii) intermediate tones often linked to free-surface reflections. Post-clustering refinements removed artifacts smaller than 200 pixels with standard morphological operations (Fig. 3 panel c)), while Canny's edge detection algorithm (Canny, 1986) enhanced flow boundaries (Fig. 3 panel d)). The resulting clusters have been used to estimate the following quantities: (I) the fraction of fluid relative to the total area in the ROI $\left(\frac{P_{fluid}}{P_{tot}}\right)$; (II) the relative amount of air pixels within the fluid region $R_a = \left(\frac{P_{air}}{P_{fluid}}\right)$ (in the following referred to as the "air content"). Both quantities were tracked over time to analyze the effect of the aeration levels on the wave impact forces, discussed later. This approach is completely non-invasive and readily configurable for different flow conditions. However, it inherently captures only two-dimensional projections, so overlapping bubbles or strong three-dimensional turbulence may lead to occasional misclassifications. Moreover, consistent lighting conditions are crucial to avoid erroneous clustering. Despite these limitations, the methodology demonstrated to be robust in accurately tracking aerated regions during wave impacts. This was confirmed by a dedicated validation process in which the clustering results were carefully compared with the raw experimental frames and cross-referenced with observable physical phenomena (Fig. 3 panel d)). Specifically, the segmented regions – air bubbles, water, and background – are in good agreement with the features actually recorded in the laboratory, ensuring that the methodology reliably captured the key aspects of the flow dynamics.

3. Results and discussion

3.1. Classification of post-overtopping events

In this section the classification of post-overtopping flow events (DB, PDB, HF) of the 52 wave tests carried for the baseline configuration (i.e., without the wave wall) is presented. It has been carried out by a visual analysis of the flow, according to the criteria reported by Greco et al. (2005, 2007), Fontes et al. (2021). Examples of the three types of events are reported in Fig. 4, where three panels containing 9 frames are presented for each event type, namely: DB (panel a)), PDB (panel b)), and HF (panel c)). Fig. 4 shows the onset of the different types of post-overtopping flows at composite vertical breakwater having the characteristics described in the literature.

Once the post-overtopping flows events have been visually classified, it is of interest to better explore their characteristics in terms of waves and structural parameters. To this end, Fig. 5 is used. In the figure, both the panels report on the x-axis the wave steepness $\left(\frac{H}{L_0}\right)$, while on the y-axis the ratio between the height of the trunk freeboard A_c (measured from the undisturbed water level) and the incident wave height H is represented. The left panel refers to the 52 baseline configuration tests, therefore $A_c = R_c$. The post-overtopping flows, previously classified, are reported with different markers, namely: DB (circles), PDB (diamonds), and HF (triangles). Three distinct regions, each pertaining to a different type of event, are visually identified with dashed black lines. Specifically, the line that separates DB from PDB is defined by the threshold $H/L_0 = 0.045$, while the one that divides PDB from HF follows the linear relation $A_c/H = -17.33(H/L_0) + 1.88$. Although the wave steepness is crucial in triggering different event types, the combined effect of this quantity and of the structure geometry governs the transition especially from PDB to HF. As previously mentioned, among these 52 tests, 15 were selected as representative wave conditions of each post-overtopping flow type, and are carried out again after installing the wave wall on top of the structure. These events are identified with red markers in the left panel.

The right panel reports the test configurations with retreated wave wall, thus $A_c = R_c - h_w$. Here are shown the selected subset of the new tests (red dots) and all the data obtained during the previous experimental campaigns, which have been retrospectively classified according to the post-overtopping flow event types. These are represented as black dots (Romano and Bellotti, 2023) and gray dots (Romano et al., 2024), respectively.

3.2. Hydrodynamic mapping of wave forces on retreated walls

In this section, the results related to the tests with the wave wall are presented and discussed, considering the subset of 15 runs repeated for three wave wall retreat configurations, obtaining a total number of 45 tests. Since regular waves are used, the results are analyzed in a time window that has a duration of one wave period. Within this window, both wave-induced loads and image-based analysis of the wave-structure interaction process are discussed.

An example of the analysis carried out is given in the Figs. 6, 7, and 8. These three figures refer to different representative post-overtopping event types selected among the subset, specifically Fig. 6 for DB, Fig. 7 for PDF and Fig. 8 for HF. Note that the classification (DB, PDB, and HF) is retained throughout the following discussion, although the presence of the wave wall would alter the evolution of post-overtopping flows compared to the baseline configuration. The figures are made of three row panels, each referring to a different G_c and organized as follows: on the left nine selected time stacks of the wave-structure interaction process captured by the camera; on the right a dual-axis plot, for which the x-axis represents the time normalized with respect to the wave period (t/T). The left y-axis reports the time series of the wave-induced forces on the wall (black line). The right y-axis displays two air-content indicators: $\frac{P_{fluid}}{P_{tot}}$ (blue line) and R_a (red line). Moreover, stars and numbers identify the selected time instant represented in the time stacks. Finally, the vertical dashed gray line refers to the time at which the maximum force on the trunk occurs ($t_{F_{T-max}}$).

This combined representation helps to visualize and interpret how the presence of the wave wall affects both the magnitude and timing of impacts, as well as the air content in the overtopping flow. In fact, compared to the baseline configuration, the post-overtopping flows encounter an obstacle that significantly alter their hydrodynamics and the air content. In the following sub-sections each event type is analyzed separately to explore the effect of the wave wall retreat position.

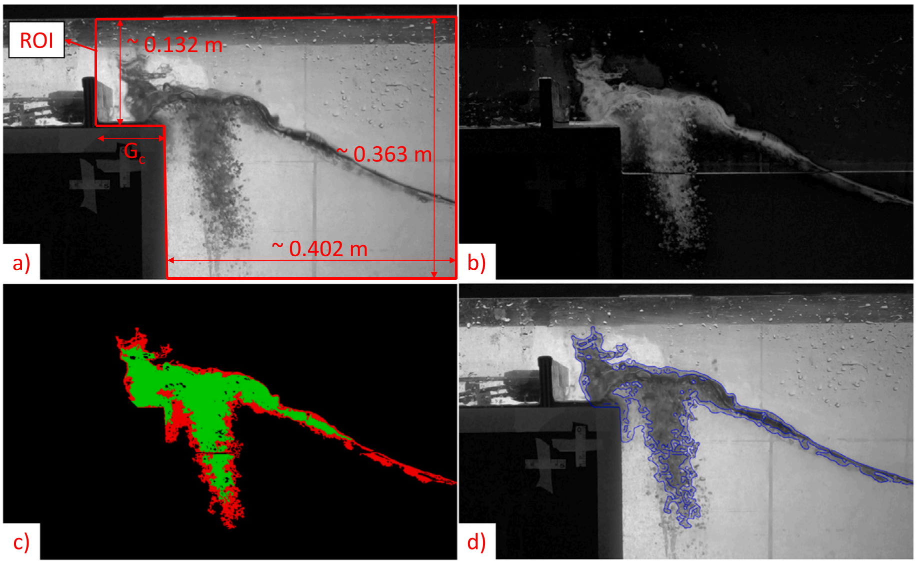

Fig. 3. Panel a): example of a gray-scale frame with ROI definition. Panel b): example of a frame after the pre-clustering optimization. Panel c): example of a frame at the end of the method (k-means algorithm). Panel d): definition of cluster edges.

3.2.1. Dam break-type events

Fig. 6, representative of a BD-type event ($H/L_0 = 0.039$, $A_c/H = 0.483$), shows, as expected, that the magnitude and timing of the force peaks on the wall vary according to the wall position. The maximum force on the wave wall ranges from about 15 N/m (G_{c3}) to 25 N/m (G_{c1} and G_{c2}). The flow exhibit a low amount of air, with an estimated air content always smaller or equal than 10% during the impact on the wall. A clear time shift between forces on the caisson trunk and on the wave wall is evident for G_{c2} and G_{c3} configurations, while for G_{c1}, the these forces appear nearly in phase.

As far as the nature of the forces signal is concerned, it should be noted that non-impulsive conditions are detected for the wall retreat positions considered. In fact, the force increases gradually and is characterized by smooth peaks. The shape of the force signal is always double-peaked, where in general the first is larger, although it can happen that the second one, caused by the jet falling back after hitting the wall exceeds the first (Peregrine, 2003; Greco et al., 2005).

3.2.2. Plunging-Dam break-type events

Fig. 7, representative of a PBD-type event ($H/L_0 = 0.082$, $A_c/H = 0.321$), shows that for this event the force peaks are significantly larger than those observed for DB. For G_{c1} it reaches a value of about 300 N/m, while it drops to around 75 N/m and 30 N/m for G_{c2} and G_{c3}, respectively. The nature of the forces signal is impulsive (church-roof-like) for G_{c1}, while it has the characteristics of a quasi-static signal for both G_{c2} and G_{c3}. This behavior is justified looking at the evolution in time of the flow. For G_{c1} the impinging jet, after overtopping the edge of the trunk, immediately clashes with the wave wall, inducing an impulsive load. Moreover, as observed for the DB-type event, the time-shift between forces on the wall and on the trunk is negligible for G_{c1}, while is relevant for increasing wall retreat G_{c2} and G_{c3}. Note that this configuration of waves and structural parameters represents one of those "worst-case scenarios" reported by Romano and Bellotti (2023) and Romano et al. (2024). In these conditions the forces acting on the wave wall, which exhibit an impulsive nature, are in phase with those acting on the trunk, inducing a general loading configuration of the structure that is way more severe than that occurring for a flushed-wall configuration under the same wave conditions.

On the contrary, for G_{c2} and G_{c3}, the increasing wall retreat, together with the interaction between the incoming and the reflected jets (see frames 4 and 25, panel b) and frame 6, panel c)), favor the dissipation of the post-overtopping flow, resulting in reduced values of the force on the wall. This behavior is consistent with the preliminary findings of Romano and Bellotti (2023). As for the air content, Fig. 7 shows that, regardless the position of the wall, it is generally larger than that observed for DB, spanning in the range 10%–25%.

3.2.3. Hammer-Fist-type events

Fig. 8, representative of a HF-type event ($H/L_0 = 0.096$, $A_c/H = 0.335$), highlights that this event type has several points in common with PDB. The force peak is rather impulsive for G_{c1}, reaching a maximum value of about 190 N/m, while drops down to 75 N/m and 50 N/m for G_{c3} and G_{c2}, respectively. This dynamics is very similar to that described for PDB and it is related to the interaction between the incoming and the reflected jets (see frames 4 and 25, panel b) and frame 4, panel c)). Also in this case the time-shift between the forces on the trunk and on the wall is not relevant for G_{c1}, although they are not perfectly in phase, due to the larger vertical component of the overtopping jet (see frame 4, panel a)) compared to that shown for PDB. This time lag is more pronounced for increasing wall retreat G_{c2} and G_{c3}. Moreover, for HF-event type the quasi-static load for G_{c2} and G_{c3} has a longer duration than that observed for PDB. Similarly to what observed for PDB, the air content is in the range 10%–25%, regardless the wall position.

3.2.4. Synthetic parameters

All the new 45 tests, carried out varying the wave wall position, have been analyzed with the same methodology of that shown in Figs. 6, 7, and 8. Therefore, for each test, some synthetic indicators, of both air content and forces, are extracted, as shown in Fig. 9, and considered for the following analysis, namely: (I) $\overline{R_a}$ is the time-average of R_a over one wave period (red dashed line in Fig. 9); (II) Δ_{R_a} is the difference between maximum and minimum values of R_a over one wave period; (III) R_a^P is the value of R_a at the time instant at which the maximum peak force occurs; (IV) $\frac{F_W^{1P}}{\rho g H^2}$ is dimensionless peak force; (V) $\frac{F_W^{1P}}{F_W^{2P}}$ is the ratio between the first and second force peaks; (VI) $\frac{t_r}{T}$ is the dimensionless rise time of the first peak.

The values of the synthetic parameters are represented in Fig. 10 in the form of scatter plots, organized in a 3 × 3 matrix form. The

a) Dam break

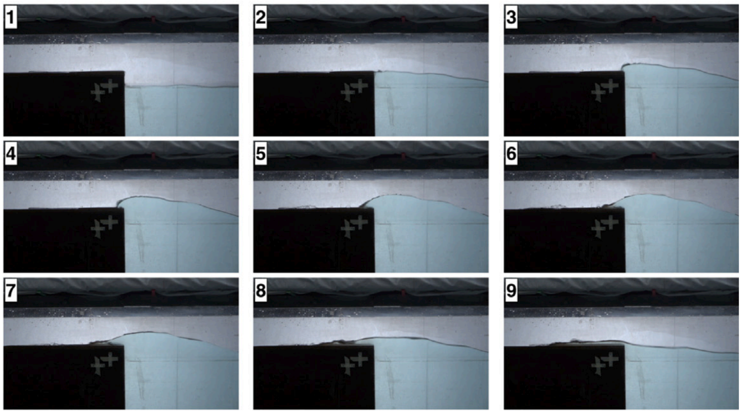

b) Plunging-Dam break

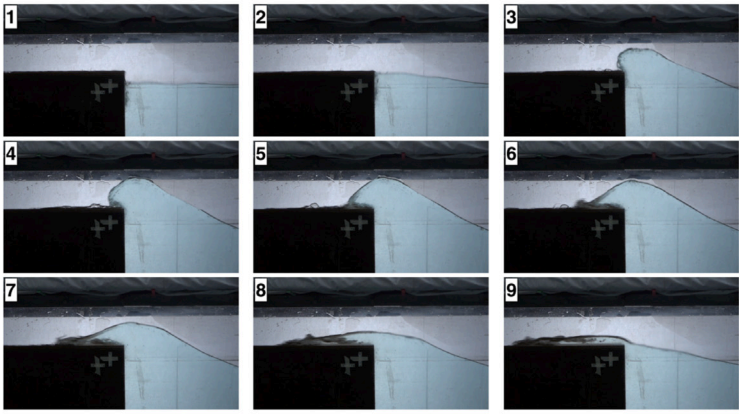

c) Hammer-Fist

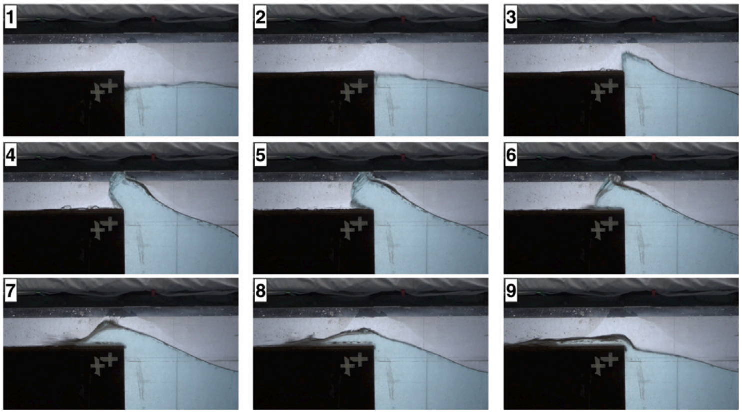

Fig. 4. Representative example of post-overtopping event-type interacting with the baseline configuration (no-wall). From top to bottom: (a) Dam break-type (H/L_0 = 0.039, $A_c/H = 0.483$) ; (b) Plunging-Dam break-type ($H/L_0 = 0.082$, $A_c/H = 0.321$) (c) Hammer-Fist-type ($H/L_0 = 0.096$, $A_c/H = 0.335$).

aim of this figure is to evaluate if a relationship exists between these six indicators. To this end, the force and the air content variables are reported on the x- and y-axis, respectively. In the figure, the markers' type refers to the post-overtopping flow event (circles for DB, diamonds for PDB, and triangles for HF), while the markers' color refers to the wall retreat position (red for G_{c1}, green for G_{c2}, and blue for G_{c3}). The dashed vertical red lines in the central column represent the value of $\frac{F_W^{1P}}{F_W^{2P}} = 1$.

Fig. 10 shows that the largest values of the force variables ($\frac{F_W^{1P}}{\rho g H^2}$ and $\frac{F_W^{1P}}{F_W^{2P}}$) are related to the PDB- and HF-type events for the G_{c1} configuration. HF-type events show the highest values of $\frac{F_W^{1P}}{F_W^{2P}}$, while PDB-type events exhibit the shortest $\frac{t_r}{T}$. Moreover, the figure shows that, in general, the air content tends to increase for increasing forces, while it shows a decreasing trend for increasing rise time. It should be noted that no clearly recognizable patterns can be identified among these synthetic parameters. Nevertheless, a fairly meaningful correlation seems to exist between $\overline{R_a}$ and $\frac{F_W^{1P}}{\rho g H^2}$ (see upper left panel). It should be mentioned that the air content indicators, although affected by a degree of uncertainty, can provide valuable estimates, useful to guide the application, and the results interpretation, of numerical models applied to simulate the hydrodynamics of such flows, especially if computational fluid dynamics (CFD) models are used. The ranges of the values of the indicators shown in Fig. 10 are reported in Table 3. Note that for DB-type events, no range is reported in the table as a single test has been carried out for each wall retreat configuration.

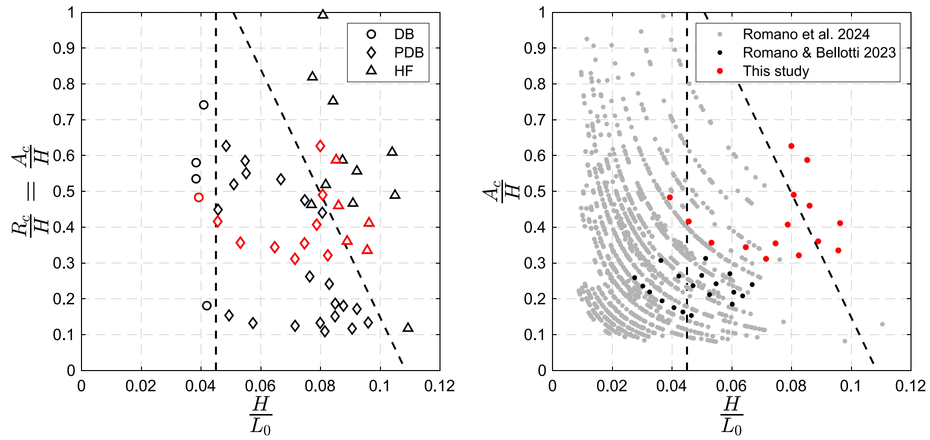

Fig. 5. Left panel: classification of the 52 new tests carried out without a wave wall (DB, circles; PDB, diamonds; HF, triangles). The dashed black lines divide the three distinct regions pertaining to each event type. Red markers identify the subset made of 15 selected representative wave conditions to be reproduced with wave wall. Right panel: selected subset of the new tests (red dots) and all the data obtained during the previous experimental campaigns (black and gray dots, respectively Romano and Bellotti, 2023; Romano et al., 2024).

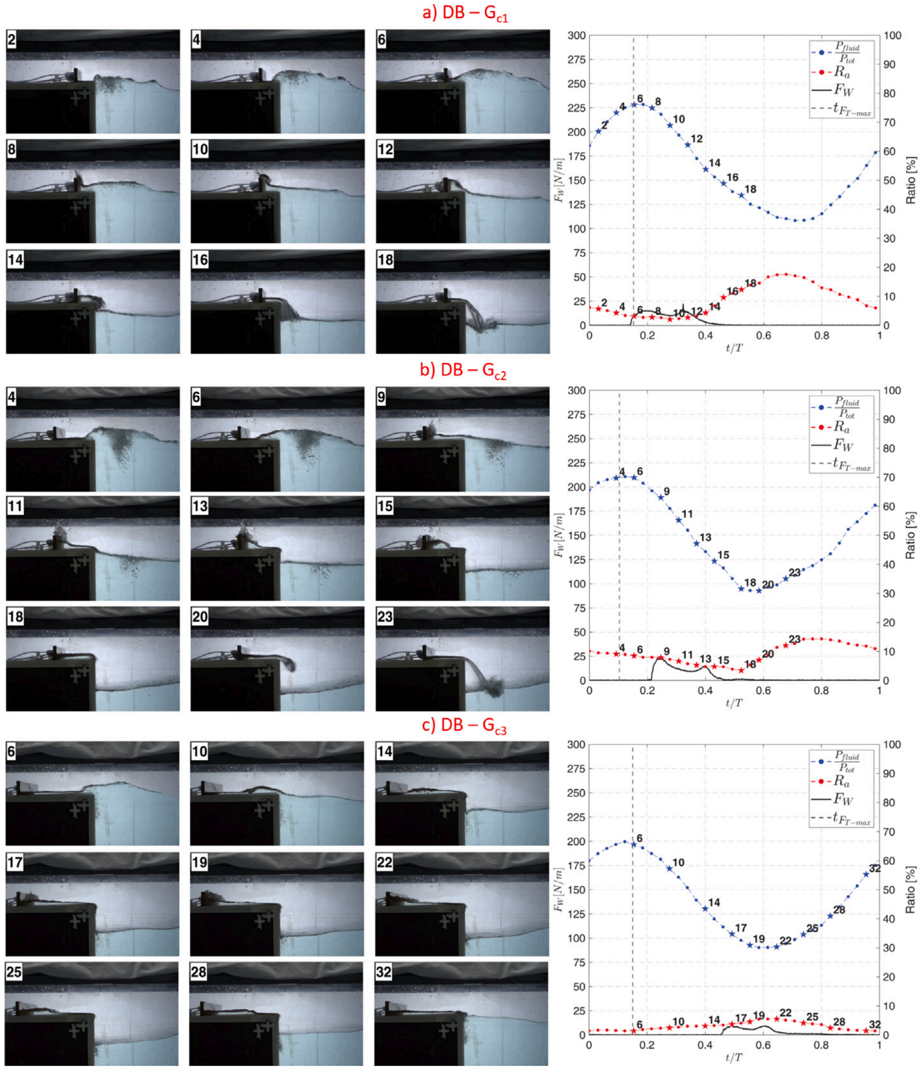

Fig. 6. Representative DB-type event ($H/L_0 = 0.039$, $A_c/H = 0.483$) across three wall retreat positions: (a) G_{c1}, (b) G_{c2}, (c) G_{c3}. Each panel shows 9 time stacks (left) and synchronized signals (right): wall force (black line), $\frac{P_{fluid}}{P_{tot}}$ (blue line), and R_a (red line). Time is normalized by T; stars mark selected frames; dashed gray line indicates the time of the peak trunk force.

a) PDB – G_{c1}

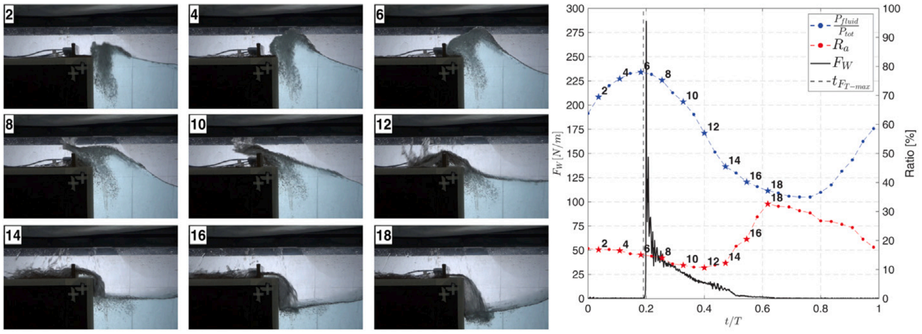

b) PDB – G_{c2}

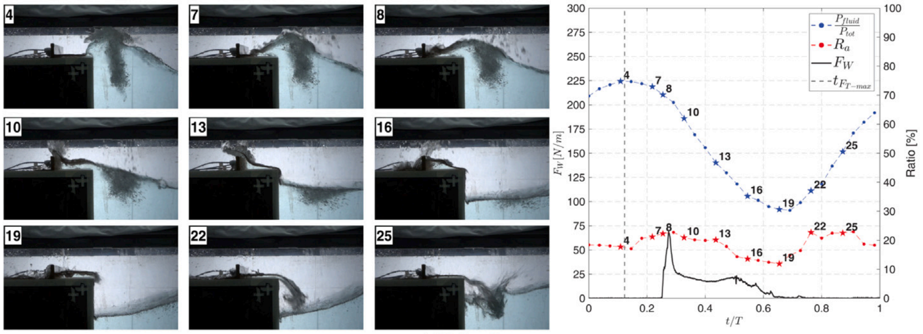

c) PDB – G_{c3}

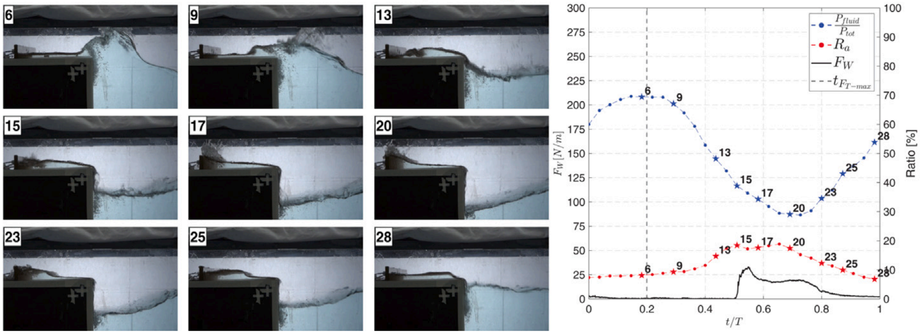

Fig. 7. Representative PDB-type event ($H/L_0 = 0.082$, $A_c/H = 0.321$) across three wall retreat positions: (a) G_{c1}, (b) G_{c2}, (c) G_{c3}. Each panel shows 9 time stacks (left) and synchronized signals (right): wall force (black line), $\frac{P_{fluid}}{P_{tot}}$ (blue line), and R_a (red line). Time is normalized by T; stars mark selected frames; dashed gray line indicates the time of the peak trunk force.

Table 3
Synthetic parameters, reported in Fig. 10, for different wall retreat distances and post-overtopping event types (DB, PDB, HF).

	G_{c1}	G_{c2}	G_{c3}
DB	$F_W^{1P}/\left(\rho g H^2\right) \approx 0.18$	$F_W^{1P}/\left(\rho g H^2\right) \approx 0.18$	$F_W^{1P}/\left(\rho g H^2\right) \approx 0.08$
	$F_W^{1P}/F_W^{2P} \approx 0.68$	$F_W^{1P}/F_W^{2P} \approx 1.44$	$F_W^{1P}/F_W^{2P} \approx 0.85$
	$t_r/T \approx 0.06$	$t_r/T \approx 0.05$	$t_r/T \approx 0.04$
	$\overline{R_a} \approx 8.70$	$\overline{R_a} \approx 9.14$	$\overline{R_a} \approx 2.96$
	$\Delta_{R_a} \approx 15.51$	$\Delta_{R_a} \approx 10.91$	$\Delta_{R_a} \approx 4.11$
	$R_a^P \approx 3.20$	$R_a^P \approx 7.87$	$R_a^P \approx 3.71$
PDB	$0.03 < F_W^{1P}/\left(\rho g H^2\right) < 1.01$	$0.03 < F_W^{1P}/\left(\rho g H^2\right) < 0.55$	$0.03 < F_W^{1P}/\left(\rho g H^2\right) < 0.27$
	$1.20 < F_W^{1P}/F_W^{2P} < 7.02$	$0.72 < F_W^{1P}/F_W^{2P} < 4.37$	$< 0.86 < F_W^{1P}/F_W^{2P} < 2.05$
	$0.01 < t_r/T < 0.07$	$0.01 < t_r/T < 0.08$	$0.02 < t_r/T < 0.05$
	$6.88 < \overline{R_a} < 20.40$	$0.80 < \overline{R_a} < 19.45$	$1.13 < \overline{R_a} < 11.81$
	$4.16 < \Delta_{R_a} < 21.97$	$0.86 < \Delta_{R_a} < 15.04$	$1.59 < \Delta_{R_a} < 12.05$
	$4.63 < R_a^P < 14.82$	$1.03 < R_a^P < 22.72$	$2.01 < R_a^P < 17.24$
HF	$0.12 < F_W^{1P}/\left(\rho g H^2\right) < 0.80$	$0.13 < F_W^{1P}/\left(\rho g H^2\right) < 0.23$	$0.05 < F_W^{1P}/\left(\rho g H^2\right) < 0.34$
	$2.72 < F_W^{1P}/F_W^{2P} < 11.03$	$0.95 < F_W^{1P}/F_W^{2P} < 3.59$	$1.01 < F_W^{1P}/F_W^{2P} < 1.79$
	$0.01 < t_r/T < 0.03$	$0.01 < t_r/T < 0.05$	$0.01 < t_r/T < 0.15$
	$5.61 < \overline{R_a} < 21.44$	$1.48 < \overline{R_a} < 18.28$	$2.72 < \overline{R_a} < 13.34$
	$5.11 < \Delta_{R_a} < 17.04$	$2.26 < \Delta_{R_a}\ 18.50$	$3.09 < \Delta_{R_a} < 10.43$
	$5.62 < R_a^P < 18.05$	$2.68 < R_a^P < 24.24$	$2.34 < R_a^P < 15.59$

a) HF – G_{c1}

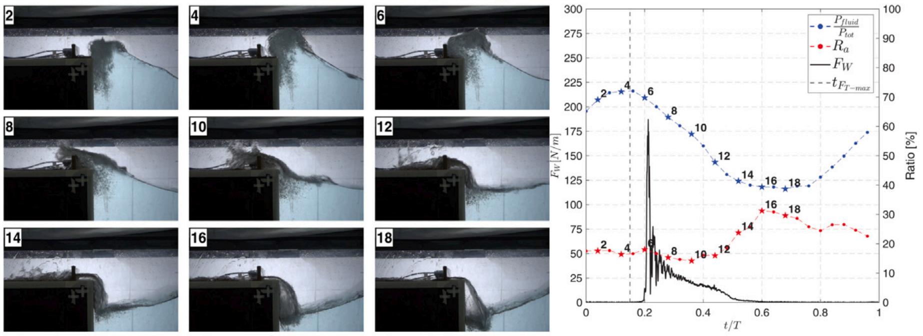

b) HF – G_{c2}

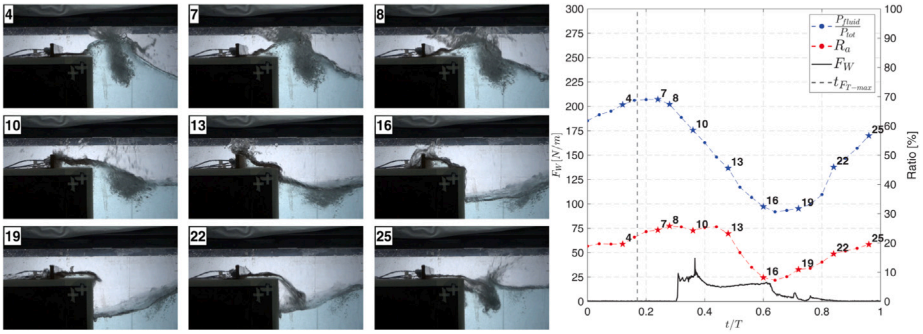

c) HF – G_{c3}

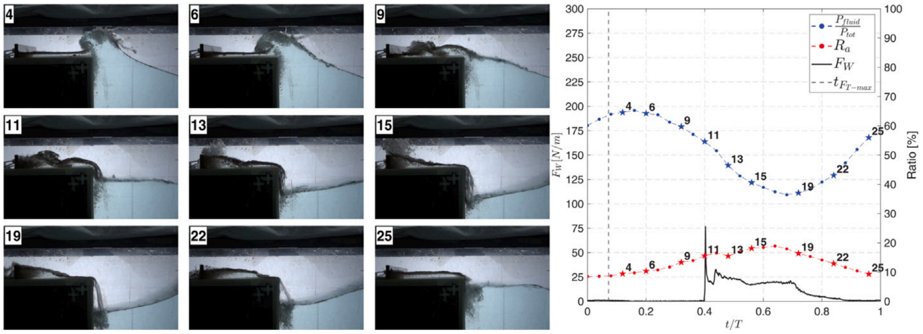

Fig. 8. Representative HF-type event (H/L_0 = 0.096, A_c/H = 0.335) across three wall retreat positions: (a) G_{c1}, (b) G_{c2}, (c) G_{c3}. Each panel shows 9 time stacks (left) and synchronized signals (right): wall force (black line), $\frac{P_{fluid}}{P_{tot}}$ (blue line), and R_a (red line). Time is normalized by T; stars mark selected frames; dashed gray line indicates the time of the peak trunk force.

3.3. Parameters map

In this section, a parameters map is presented to summarize the results previously described and to contribute developing practical design tools for composite vertical breakwaters with retreated wall in deep-water conditions. Both the purpose and the structure of this map are inspired to the PROVERBS parameters map proposed by Oumeraci et al. (2001). Nevertheless, the present map refers to loads acting on the wave wall when placed on a retreated position with respect to the seaward face of the caisson.

The purpose of the map is to guide the design of these structures, providing a tool to estimate the forces acting on the wall, given the waves and structure geometry parameters. Fig. 11 shows the structure of the map, which is organized in three rows. The first row depicts the sketch of the cross section with governing waves and geometrical parameters. The second row presents the proposed fitting curves and the 95% error bounds for estimating the peak value of wave force on the wall, while the third row shows the shape of the dimensionless force time series.

The process for using the map can be summarized in the following workflow: the first step (see first row) consists in identifying the post-overtopping event type (DB, PDB, or HF) depending on both H/L_0 and A_c/H, as proposed in Fig. 5. In this regard, if $H/L_0 < 0.045$ the event is classified as DB, if $H/L_0 > 0.045$ and $Ac/H < -17.33(H/L_0) + 1.88$ the event is classified as PDB, finally if $H/L_0 > 0.045$ and $Ac/H > -17.33(H/L_0) + 1.88$ the event is classified as HF.

Depending on the dominant event type, the map divides into three distinct branches. For each branch it is possible to calculate, depending on G_c, the dimensionless peak value of wave forces on the wall ($\frac{F_W}{\rho g H^2}$) using a proposed fitting formula as a function of the dimensionless parameter $\frac{R_c G_c}{H h_w}$ (see second row). The formula reads as follows:

$$\frac{F_W}{\rho g H^2} = \exp\left(\alpha \frac{R_c G_c}{H h_w}\right) + \beta, \tag{2}$$

where $\alpha = -0.06$ and $\beta = 0.7634$. It should be noted that Eq. (2), represented by a red dashed line in the figure, has been obtained by fitting the new experiments combined with all the data collected during the previous experimental campaigns on composite vertical breakwaters with retreated wall (Romano and Bellotti, 2023; Romano et al., 2024). The present formula is valid within the following parameters' range: $0.08 \leq A_c/H \leq 0.99$, $0.01 \leq H/L_0 \leq 0.11$, and $0.03 \leq G_c/L_0 \leq 0.35$. The entire dataset is represented with gray dots, and the black markers highlight the data related to each post-overtopping event type for the specific branch. The blue dashed lines represent the error bounds of

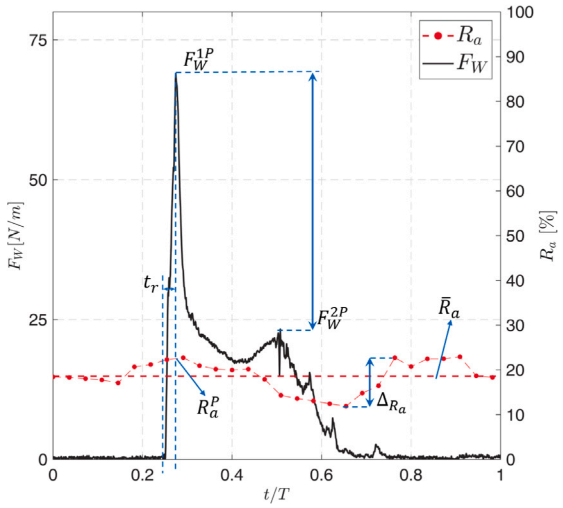

Fig. 9. Definition of synthetic parameters from force on the wall (black line) and air content (red dashed line) signals over a wave period.

95%. Notice that the presented fitting exhibits a significant data scatter ($R^2 = 0.085$). Nevertheless, it should be pointed out that the variability of impulsive impacts is well recognized in the literature. In fact, similar observations have been widely reported in previous studies on wave impact forces (Stagonas et al., 2016; Marzeddu et al., 2017; Raby et al., 2022), where the inherently chaotic nature of wave impacts, combined with the role of air entrainment in wave-structure interaction, lead to significant variability in measured loads. As also noted by Peregrine (2003), Bullock et al. (2007) and Hofland et al. (2010), the lack of repeatability is not merely an experimental limitation but a physical characteristic of impulsive wave impacts, strongly influenced by transient flow features, residual motions, and even the presence of micro-scale instabilities near the crest tip (Lubin et al., 2019; Meerkerk et al., 2021).

Moreover, since often structural dynamic analysis is required to properly design such structures under impulsive loads, it is important to have an idea of the nature of the force time series acting on the wall. Thus, the proposed map allows to estimate the shape of the dimensionless force time series. Specifically, within each branch (i.e., event type) the map distinguishes three levels of wave wall retreat: small ($0.5 < G_c/H < 1$), medium ($1 \leq G_c/H \leq 2.2$), and large ($2.2 < G_c/H < 4.5$). For each level of wall retreat, within each event type, a dimensionless force time series acting on the wave wall is provided in the figures of the third row. The data represented in the figures are extracted from the present experimental campaign and are represented as a function of t/T with gray lines, while their average value in time is shown with red lines.

Finally, it is of interest to relate the range of parameters explored to derive the present map with that investigated within the PROVERBS parameters map. The purpose is not to compare the two maps, but to provide an opportunity for future adjustments and/or extensions of the present map eventually referring to different structure arrangements, irregular waves, etc. Therefore, the PROVERBS parameters $h_b^* = h_b/h$ and $H_s^* = H_s/h$, related to the present test campaign, are as follows: $0.3 < h_b^* < 0.6$ (Low Mound Breakwater), under Small ($0.1 < H_s^* < 0.2$) to Large Waves ($0.2 < H_s^* < 0.6$). Note that these parameters, originally defined for irregular waves (H_s), are calculated using the regular wave height (H).

3.4. Downfall pressures

Finally, this section presents the analysis of the downfall pressures. Despite their potential significance in structural loading, particularly important under impulsive overtopping conditions, these pressures have received limited attention in traditional design guidelines and only few studies are available on the topic (Wolters et al., 2005).

Downfall pressures have been measured for all the tests carried out during the present campaign. Fig. 12 illustrates the asynchronous maximum pressure (P_{df}) diagrams of both frontal and downfall pressures obtained for each event type and for both baseline and retreated wall configurations. The tests represented in the figure have been selected, among the whole dataset, according to the maxima values of the downfall pressures. The three columns represent the different event types: DB, PDB, and HF (first, second, and third column, respectively). Each row refers to the baseline (i.e., no wave wall), G_{c1}, G_{c2}, and G_{c3} configurations (first, second, third and fourth row, respectively). In each panel, the x- and y-axis are expressed in terms of both spatial scale in meters and meters of water column (all the values refer to laboratory scale); the black lines represent the structure geometry, the blue lines indicate the still water level, the gray circles identify the positions of the pressure sensors, the red lines represent recorded values of pressures, and the gray dashed lines represent the pressures calculated using Goda's formulae (Goda, 2010) for the considered wave conditions.

As reported in Fig. 12, the presence of the wave wall changes the dynamics of the downfall pressures. For DB-type events the downfall pressures exhibit a slight increase both in front and behind the wall for G_{c1} and G_{c2}, while for G_{c3} the loading pattern is very similar to the baseline configuration. For PDB-type events, which conversely to DB are characterized by a large vertical momentum component, the downfall pressure are significant for every configuration. The worst loading is noticed for G_{c1}, where large pressures occur both in front and behind the wall. A similar pattern of downfall pressures, is noticed for HF-type events where the largest value occur for the baseline configuration and G_{c1}.

To summarize, as a general result it appears that, regardless the event type, the downfall pressures increase both in front and behind the wall for small/medium retreats, while for large retreats the downfall pressures pattern is milder. Finally, it should be mentioned that the severest loading conditions occur for PDB and HF when the wall retreat is small. Table 4 summarizes the maxima downfall pressure values obtained for every event type and wall configuration in dimensionless form ($P_{df}^{max}/\rho g H$), following the approach proposed by Wolters et al. (2005), who reported maxima values in the order of $12\rho g H$. It should be noted that the downfall pressures values for retreated wall configurations range between $0.35\rho g H$ (DB) and $4.51\rho g H$ (HF). Therefore, their order of magnitude is coherent with that mentioned by Wolters et al. (2005), although their work refers to impacts of breaking waves in shallow waters on a pure vertical structure with no wave wall on top.

3.5. Limitations

While the present study offers new insights into the hydrodynamics of post-overtopping flows on composite vertical breakwaters with retreated wave wall, some limitations should be considered when interpreting the results. The experiments were carried out in a 2D wave flume using fresh water and scaled conditions. These factors may introduce scale effects, particularly in processes involving air entrainment and compressibility during wave impacts that might vary under full-scale and saltwater conditions. These phenomena have been largely studied in the literature and the following effects have been pointed out: e.g., the aeration levels affect the pressure rise times and peak pressures during violent wave impacts (Bullock et al., 2001; Chang et al., 2011). Moreover, the compressibility of air and the subsequent "bounce back" effect during wave impacts demonstrated that compressed air pockets or clusters of bubbles could amplify impact pressures significantly (Wood et al., 2000). Additionally, Hattori et al. (1994), Calabrese and Vicinanza (1999), and Cox and Shin (2003)

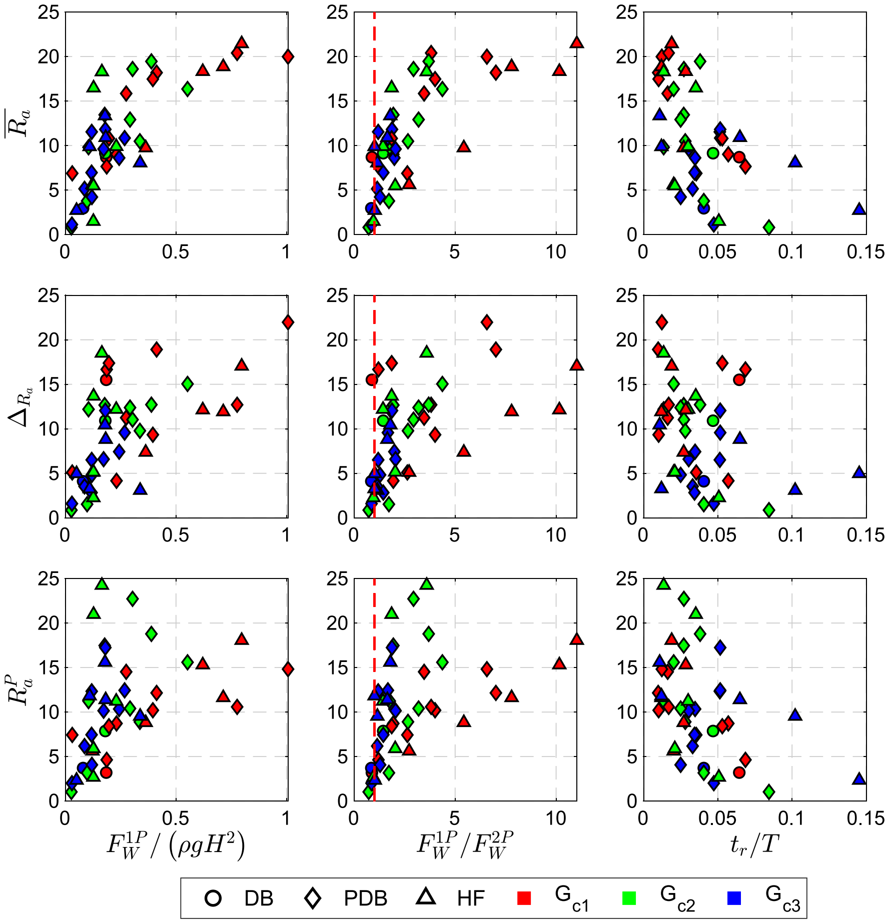

Fig. 10. Synthetic parameters map for classifying post-overtipping flow events and predicting impulsive loads on composite breakwaters with retreated wave walls.

Table 4
Summary of maximum vertical downfall pressures ($P_{df}^{max}/\rho g H$) recorded during different overtopping events (DB, PDB, HF) as a function of the incident wave height and wave wall retreat distances.

	No-wall	Small retreat $0.5 < \frac{G_c}{H} < 1$	Medium retreat $1 \leq \frac{G_c}{H} \leq 2.2$	Large retreat $2.2 < \frac{G_c}{H} < 4.5$
Dam break	0.46	0.94	0.85	0.35
Plunging-Dam break	3.36	3.56	1.96	1.38
Hammer-Fist	4.71	4.51	2.21	1.05

showed that a certain degree of aeration could cushion direct impact forces, but larger, more densely compressed air bubbles could generate pressure spikes.

Comparisons between laboratory and field measurements have revealed significant differences in impact behavior between waves breaking in freshwater and seawater. Bullock et al. (2001) demonstrated that the void fraction in seawater is an order of magnitude greater than in freshwater under similar conditions. The persistence of smaller but more numerous air bubbles in seawater complicates pressure analyses, as also highlighted by Blenkinsopp and Chaplin (2007, 2011). Field observations by Blackmore and Hewson (1984) noted discrepancies between measured and theoretical impact pressures, which were attributed to factors like air entrapment, wave steepness, celerity, and period. Small-scale laboratory experiments, particularly those in freshwater, face challenges related to scale effects. It should be mentioned that small-scale experiments carried out using freshwater instead of seawater are characterized by the presence of smaller bubbles with a decreased lifetime, and lower air entrainment (Stagonas et al., 2011). The buoyancy and compressibility of aerated green water flows are not well represented in small-scale laboratory experiments, leading to limitations in accurately reproducing large-scale flow behavior and air entrainment characteristics (Kobus and Koschitzky, 1991; Chanson et al., 2006). Bullock et al. (2001) also highlighted that bubbles in controlled environments differ in size and behavior from those in the open sea, limiting the applicability of Froude scaling for precise replication of full-scale phenomena. Despite these challenges, research by Deane and Stokes (1999, 2002) found similarities in bubble size distributions between laboratory and oceanic breaking waves, suggesting consistent bubble formation mechanisms. Kobus and Koschitzky (1991) also noted that bubble sizes in aerated flows remained consistent across scales, supporting the validity of some physical models used in engineering predictions.

Another limitation consists in using regular waves. This decision was made following the previous approach of Romano and Bellotti (2023), Romano et al. (2024). In fact, the wave impacts, which are object of the study, are characterized by a large variability and uncertainty, also related to the aspects previously mentioned. Therefore, in order to focus on the physics of the post-overtopping flows, regular waves are used and the related phenomena are investigated over one wave period (i.e., intra-wave analysis). As a result, the outputs

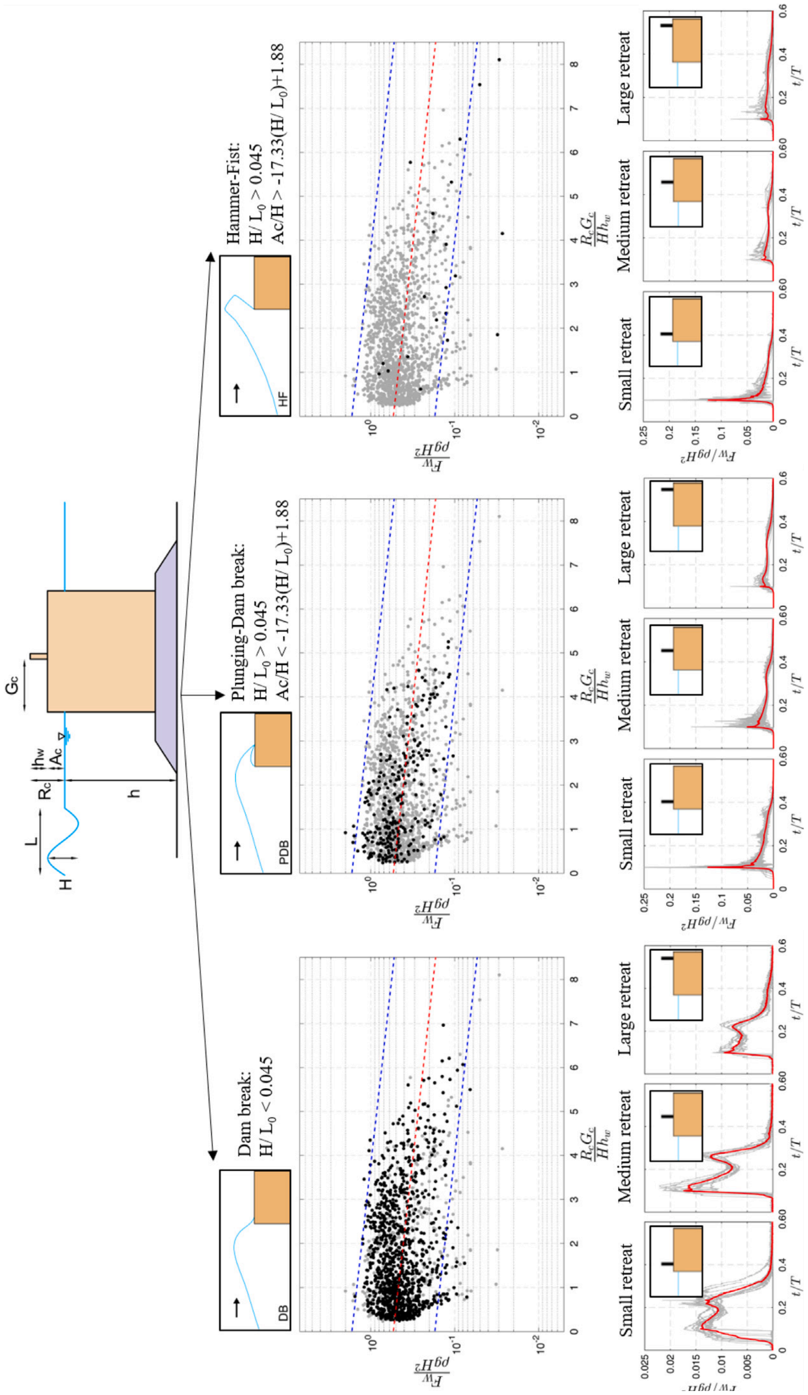

Fig. 11. Asynchronous maximum pressure diagrams of both frontal and downfall pressures. The three columns represent the different event types: DB, PDB, and HF (first, second, and third column, respectively). Each row refers to the baseline (i.e., no wave wall), G_{c1}, G_{c2}, and G_{c3} configurations (first, second, third and fourth row, respectively). In each panel, the x- and *y*-axis are expressed in terms of both spatial scale in meters and meters of water column (values in laboratory scale); the black lines represent the structure geometry, the blue lines indicate the still water level, the gray circles identify the positions of the pressure sensors, the red lines represent recorded values of pressures, and the gray dashed lines represent the pressures calculated using Goda's formulae (Goda, 2010).

cannot be directly used to estimate the effects of irregular sea states on such structures. Nevertheless, they remain valid for studying the hydraulic performances of these types of breakwaters under identical, even though regular, wave conditions, as done in previous studies on vertical breakwaters (Martinelli et al., 2018; Castellino et al., 2021).

Furthermore, the structure was modeled as perfectly rigid, thus neglecting any potential influence of structural flexibility or local deformations on the distribution and intensity of impact pressures. At full scale, material compliance may mitigate or amplify pressure peaks, especially under highly impulsive loads. Moreover, the experiments were conducted in a 2D setup, which does not capture eventual 3D effects.

Finally, a limitation can be related to the image-clustering technique used to estimate air content. In fact, although this technique is non-invasive, it has some limitations: (I) the method only captures 2D view of the flow, so it might wrongly detect some regions due to overlapping bubbles or strong three-dimensional turbulence; (II) the precision of clustering results can be sensitive to lighting conditions, particularly

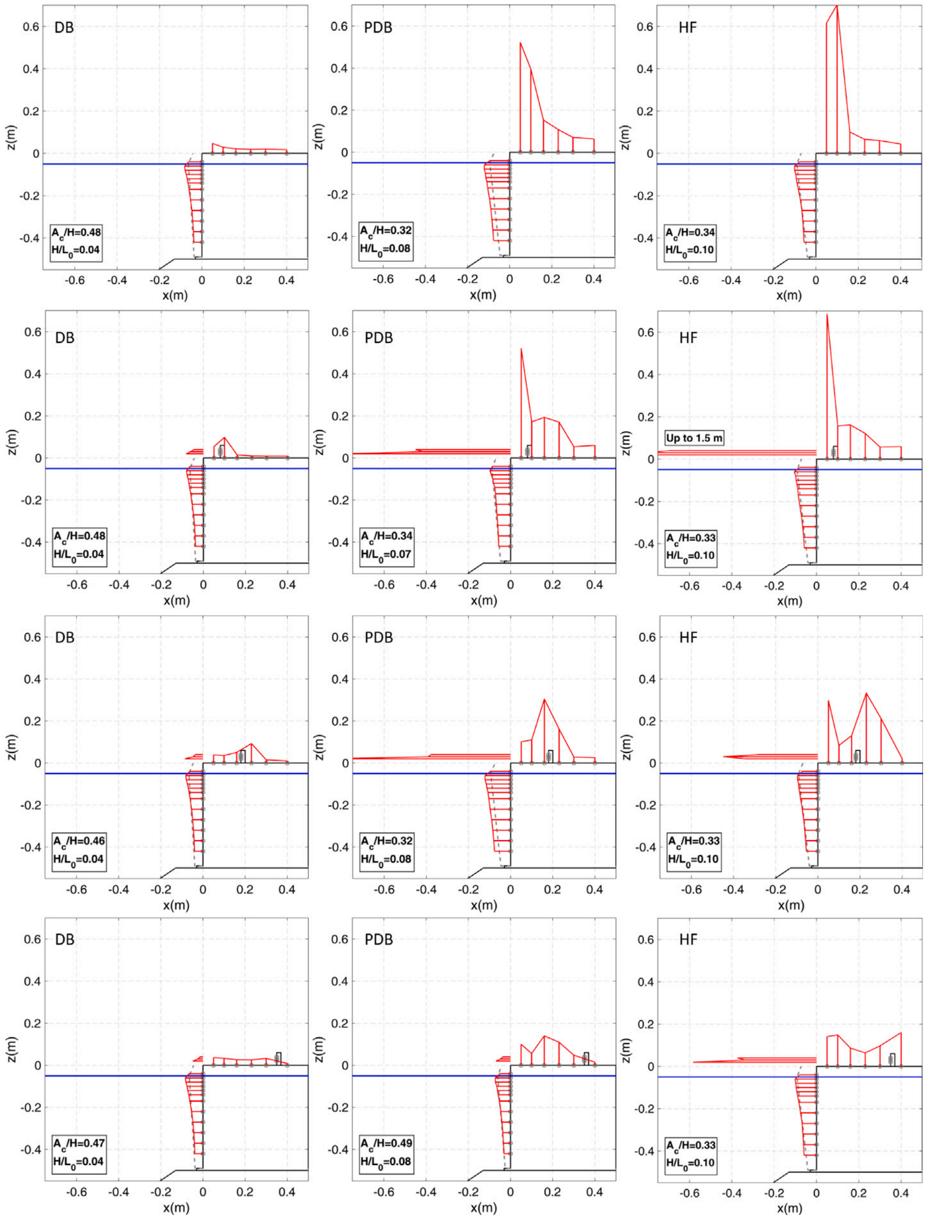

Fig. 12. Scatter plots of synthetic force and air content indicators from all 45 impact events. Marker shape indicates event type (circles: DB, diamonds: PDB, triangles: HF); marker color denotes wall retreat position (red: G_{c1}, green: G_{c2}, blue: G_{c3}).

in highly aerated and reflective scenarios. However, even if affected by a degree of uncertainty, such estimates of air content can still provide valuable input for the calibration and validation of numerical models. Despite these limitations, the experimental framework developed in this study provides a reliable basis for investigating the influence of retreated wave walls on wave-structure interaction.

4. Conclusions

In this article, a new 2D experimental campaign to explore the hydrodynamics of post-overtopping flows on composite vertical breakwaters with retreated wave walls has been presented. The experiments, carried out using regular waves, have been performed in two stages: firstly, post-overtopping flows have been studied for a structure without the wave wall (i.e., baseline configuration), in order to be classified into three main event types (DB, PDB, and HF), according to a classification proposed in the literature by Greco et al. (2005, 2007), Fontes et al. (2021) for flows on ships' decks. The experiments demonstrated that the same types of events also occur for composite vertical breakwaters. Moreover, criteria have been provided to predict the onset of specific event types based on wave characteristics and structural parameters.

In the second stage of the experimental campaign, some selected representative conditions of each event type have been reproduced, by varying the wave wall retreat position, in order to investigate how different flow event types and wall retreats affect the nature of impact loads on the structure. Therefore, during the experiments, pressures acting both on the wave wall and on the superstructure's deck have been measured and analyzed. Moreover, an optimized camera setup was specifically designed to record the hydrodynamics of post-overtopping flows and to estimate some quantities that are difficult to measure with direct measurements (e.g., air content). Then, an advanced image-clustering analysis technique has been applied to investigate in detail the processes occurring over a wave period.

The analysis of the experimental results pointed out that, depending on the wall's position, the hydrodynamic forces and characteristics vary significantly for a given event type. Specifically, the most critical loading configurations for the wave wall were observed for PDB- and HF-type events with small wall retreat ($0.5 < G_c/H < 1$). These results, confirm and extend previous findings pointed out by Romano and Bellotti (2023) and Romano et al. (2024), who highlighted the occurrence of those "worst-case scenarios". In those conditions the impulsive forces acting on the wave wall, might be in phase with those acting on the trunk, thus leading to a general loading combination on the structure that is way more severe than that occurring for a flushed-wall configuration under the same wave conditions.

Finally, the new results of wave forces acting on the wave wall, combined with the previous data of Romano and Bellotti (2023), Romano et al. (2024), retrospectively analyzed and classified in terms of post-overtopping flow types, have been used to define a parameters map. The aim of this map, which is inspired to the structure of the PROVERBS map proposed by Oumeraci et al. (2001), is to contribute to develop practical design tools for composite vertical breakwaters with retreated wall in deep-water conditions. Specifically, the map, which branches out depending on the post-overtopping flow type and wall position, allows to estimate the loads acting on the retreated wave wall, given the waves and geometrical parameters. Moreover, since often structural dynamic analysis is required to properly design such structures under impulsive loads, the map also provides the dimensionless time series of the force.

Finally, the analysis of the downfall pressures has pointed out that the presence and the position of the wave wall changes dramatically also the nature of these vertical loads. Specifically, the worst loading configuration is noticed for PDB- and HF-type events with small wall retreats ($0.5 < G_c/H < 1$), where large pressure values (up to $4.51\rho g H$) occur on the superstructure deck.

CRediT authorship contribution statement

Matteo Centorami: Writing – review & editing, Writing – original draft, Software, Investigation, Formal analysis, Data curation. **Alessandro Romano:** Writing – review & editing, Writing – original draft, Supervision, Formal analysis, Data curation, Conceptualization. **Claudia Cecioni:** Writing – review & editing, Writing – original draft, Supervision, Formal analysis, Data curation, Conceptualization. **Giorgio Bellotti:** Writing – review & editing, Writing – original draft, Supervision, Formal analysis, Data curation, Conceptualization.

Declaration of competing interest

The authors declare the following financial interests/personal relationships which may be considered as potential competing interests: co-author Giorgio Bellotti serves as Associate Editor of this journal. If there are other authors, they declare that they have no known competing financial interests or personal relationships that could have appeared to influence the work reported in this paper.

Acknowledgments

A special acknowledgment is due to the master's student Matteo Scaramozzino for the help provided during the experimental campaign.

Data availability

Data will be made available on request.

References

Aalborg University, A., 2018. Awasys 7 [www document]. www.hydrosoft.civil.aau.dk/awasys.
Andersen, T.L., Clavero, M., Eldrup, M.R., Frigaard, P.B., Losada, M., 2018. Active absorption of nonlinear irregular waves. In: Coastal Engineering 2018, Coastal Engineering Research Council.
Andersen, T.L., Clavero, M., Frigaard, P., Losada, M., Puyol, J., 2016. A new active absorption system and its performance to linear and non-linear waves. Coast. Eng. 114, 47–60.
van Bergeijk, V.M., Warmink, J.J., Hulscher, S.J., 2022a. The wave overtopping load on landward slopes of grass-covered flood defences: Deriving practical formulations using a numerical model. Coast. Eng. 171, 104047.
van Bergeijk, V.M., Warmink, J.J., Hulscher, S.J., 2022b. The effects of transitions in cover type and height on the wave overtopping load on grass-covered flood defences. Appl. Ocean Res. 125, 103220.
Blackmore, P.A., Hewson, P.J., 1984. Experiments on full-scale wave impact pressures. Coast. Eng. 8 (4), 331–346.
Blenkinsopp, C., Chaplin, J., 2007. Void fraction measurements in breaking waves. Proc. R. Soc. A: Math. Phys. Eng. Sci. 463 (2088), 3151–3170.
Blenkinsopp, C., Chaplin, J., 2011. Void fraction measurements and scale effects in breaking waves in freshwater and seawater. Coast. Eng. 58, 417–428.
Buchner, B., 1995. On the impact of green water loading. In: The Sixth International Symposium on Practical Design of Ships and Mobile Units. PRADS 1995, Seoul, South Korea, Sept, vol. 1, pp. 7–22.
Buchner, B., 2002. Green Water on Ship-Type Offshore Structures (Ph.D. thesis). Delft University of Technology Delft, The Netherlands.
Bullock, G., Crawford, A., Hewson, P., Walkden, M., Bird, P., 2001. The influence of air and scale on wave impact pressures. Coast. Eng. 42, 291–312.
Bullock, G., Obhrai, C., Peregrine, D., Bredmose, H., 2007. Violent breaking wave impacts. part 1: Results from large-scale regular wave tests on vertical and sloping walls. Coast. Eng. 54, 602–617.
Calabrese, M., Vicinanza, D., 1999. Prediction of wave impact occurrence on vertical and composite breakwaters. In: Excerpta of the Italian Contributions To the Field of Hydraulic Engineering. CUEN, Napoli, Italia, vol. XIII, pp. 91–122.
Canny, J., 1986. A computational approach to edge detection. IEEE Trans. Pattern Anal. Mach. Intell. PAMI- 8, 679–714.
Cao, D., Tan, W., Yuan, J., 2022. Assessment of wave overtopping risk for pedestrian visiting the crest area of coastal structure. Appl. Ocean Res. 120, 102985.
Castellino, M., Romano, A., Lara, J.L., Losada, I.J., Girolamo, P.De., 2021. Confined-crest impact: Forces dimensional analysis and extension of the goda's formulae to recurved parapets. Coast. Eng. 163, 103814.
Chang, K.A., Ariyarathne, K., Mercier, R., 2011. Three-dimensional green water velocity on a model structure. Exp. Fluids 51 (2), 327–345.
Chanson, H., Aoki, S., Hoque, A., 2006. Bubble entrainment and dispersion in plunging jet flows: freshwater vs. seawater. J. Coast. Res. 22 (3), 664–677.
Chen, L., Taylor, P.H., Draper, S., Wolgamot, H., 2019. 3-d numerical modelling of greenwater loading on fixed ship-shaped fpsos. J. Fluids Struct. 84, 283–301.
Chen, H., Yuan, J., Cao, D., Liu, P.L.F., 2021. Wave overtopping flow striking a human body on the crest of an impermeable sloped seawall. part ii. Numer. Model. Coast. Eng. 168, 103892.
Cox, D.T., Shin, S., 2003. Laboratory measurements of void fraction and turbulence in the bore region of surf zone waves. J. Eng. Mech. 129 (10), 1197–1205.
De Finis, S., Romano, A., Bellotti, G., 2020. Numerical and laboratory analysis of post-overtopping wave impacts on a storm wall for a dike-promenade structure. Coast. Eng. 155, 103598.
Deane, G.B., Stokes, M.D., 1999. Air entrainment processes and bubble size distributions in the surf zone. J. Phys. Oceanogr. 29, 1393–1403.
Deane, G.B., Stokes, M.D., 2002. Scale dependence of bubble creation mechanisms in breaking waves. Nature 418, 839–844.
Fontes, J.V.H., Hernández, I.D., Mendoza, E., Silva, R., Silva, E.Brandão.da., Sousa, M.Rocha.de., Gonzaga, J., Kamezaki, R.S.F., Torres, L., Esperança, P.T.T., 2021. On the evolution of different types of greenwater events. Water 13 (1148).
Formentin, S.M., Altomare, C., Marzeddu, A., Zanuttigh, B., 2024. Image clustering for overtopping volume measurements. Phys. Fluids 36, 065137.
Gao, M., Draper, S., Wolgamot, H.A., Chen, L., Taylor, P.H., Cheng, L., 2025. Green water loads on prismatic obstacles. J. Fluid Mech. 1004 (A8).
Goda, Y., 2010. Random seas and design of maritime structures, vol. 33, World Scientific Publishing Company.
Goda, K., Miyamoto, T., 1976. A study of shipping water pressure on deck by two-dimensional ship model tests. J. Soc. Nav. Archit. Jpn. 140, 16–22.
Greco, M., Colicchio, G., Faltinsen, O.M., 2007. Shipping of water on a two-dimensional structure. part 2. J. Fluid Mech. 581, 371–399.
Greco, M., Faltinsen, O.M., Landrini, M., 2005. Shipping of water on a two-dimensional structure. J. Fluid Mech. 525, 309–332.
Hattori, M., Arami, A., Yui, T., 1994. Wave impact pressure on vertical walls under breaking waves of various types. Coast. Eng. 22, 79–114.
Hofland, B., Kaminski, M., Wolters, G., 2010. Large scale wave impacts on a vertical wall. In: Proceedings of the 32nd International Conference on Coastal Engineering. Shanghai, China.

Kobus, H., Koschitzky, H.P., 1991. Local surface aeration at hydraulic structures. In Air Entrain. Free- Surf. Flows IAHR Hydraul. Des. Struct. Ser. 4, 29–53.

Lee, G.N., Jung, K.H., Malenica, S., Chung, Y.S., Suh, S.B., Kim, M.S., Choi, Y.H., 2020. Experimental study on flow kinematics and pressure distribution of green water on a rectangular structure. Ocean Eng. 195, 106649.

Lee, H.H., Lim, H.J., Rhee, S.H., 2012. Experimental investigation of green water on deck for a cfd validation database. Ocean Eng. 42, 47–60.

Lubin, P., Kimmoun, O., Véron, F., Glockner, S., 2019. Discussion on instabilities in breaking waves: vortices, air-entrainment and droplet generation. Eur. J. Mech. B Fluids 73, 144–156.

Martinelli, L., Ruol, P., Volpato, M., Favaretto, C., Castellino, M., Girolamo, P.De., Franco, L., Romano, A., Sammarco, P., 2018. Experimental investigation on non-breaking wave forces and overtopping at the recurved parapets of vertical breakwaters. Coast. Eng. 141, 52–67.

Marzeddu, A., Oliveira, T.C.A., Gironella, F.X., Sánchez-Arcilla, A., 2017. Variability of wave impact measurements on vertical breakwaters. J. Hydraul. Res. 55, 772–786.

Meerkerk, M.van., Poelma, C., Hofland, B., Westerweel, J., 2021. Gas flow dynamics over a plunging breaking wave prior to impact on a vertical wall. Eur. J. Mech. B Fluids.

Neves, M.G., Didier, E., Brito, M., Clavero, M., 2021. Numerical and physical modelling of wave overtopping on a smooth impermeable dike with promenade under strong incident waves. J. Mar. Sci. Eng. 9 (865).

Oumeraci, H., Kortenhaus, A., Allsop, W., Groot, M.de., Crouch, R., Vrijling, H., Voortman, H., 2001. Probabilistic Design Tools for Vertical Breakwaters. CRC Press.

Peregrine, D., 2003. Water-wave impact on walls. Annu. Rev. Fluid Mech. 35, 23–43.

Raby, A., Bullock, G., Jonathan, P., Randell, D., Whittaker, C., 2022. On wave impact pressure variability. Coast. Eng. 177, 104168.

Romano, A., Bellotti, G., 2023. Wave forces on vertical caissons with retreated wall: A first experimental insight. Coast. Eng. 186, 104396.

Romano, A., Centorami, M., Cecioni, C., Bellotti, G., 2024. A physical model study on the hydraulic performances of vertical breakwaters with retreated wave walls. Coast. Eng. 191, 104539.

Ryu, Y., Chang, K.A., Mercier, R., 2007. Runup and green water velocities due to breaking wave impinging and overtopping. Exp. Fluids 43, 555–567.

Silva, D.F.C., Esperança, P.T.T., Coutinho, A.L.G.A., 2017. Green water loads on fpsos exposed to beam and quartering seas. Part Ii: Cfd Simulations. Ocean. Eng. 140, 434–452.

Song, Y.K., Chang, K.A., Ariyarathne, K., Mercier, R., 2015. Surface velocity and impact pressure of green water flow on a fixed model structure in a large wave basin. Ocean Eng. 104, 40–51.

Stagonas, D., Marzeddu, A., Gironella, F.X., Sánchez-Arcilla, A., Muller, G., 2016. Measuring wave impact induced pressures with a pressure mapping system. Coast. Eng. 112, 44–56.

Stagonas, D., Warbrick, D., Muller, G., Magagna, D., 2011. Surface tension effects on energy dissipation by small scale, experimental breaking waves. Coast. Eng. 58, 826–836.

Takahashi, S, 1996. Design of vertical breakwaters. breakwater design. In: International Conference on Coastal Engineering. Orlando, Short Course.

Wang, H., Santo, H., Taylor, P.H., Dai, S.S., Chan, E.S., 2023. Experimental and numerical study of wave-in-deck loads due to oblique transient wave groups. J. Fluids Struct. 120, 103914.

Wolters, G., Müller, G., Bruce, T., Obhrai, C., 2005. Large-scale experiments on wave downfall pressures. Proc. Inst. Civ. Eng. - Marit. Eng. 158 (MA4) 13, 7–145.

Wood, D., Peregrine, D., Bruce, T., 2000. Wave impact on a wall using pressure-impulse theory. i: trapped air. J. Waterw. Port Coast. Ocean. Eng. 126, 182–190.